Mon. Not. R. Astron. Soc. **000**, 1–9 (2016) Printed 29 June 2016 (MN LATEX style file v2.2)

Could Segue 1 be a destroyed star cluster? – a dynamical perspective

R. Domínguez[1⋆], M. Fellhauer[1], M. Blaña[2], J.P. Farias[1], J. Dabringhausen[1], G.N. Candlish[1], R. Smith[3] and N. Choque[1]

[1] *Departamento de Astronomía, Universidad de Concepción, Casila 160-C, Concepción, Chile*
[2] *Max-Planck-Institut fr extraterrestrische Physik, Giessenbachstrasse 1, D-85748 Garching, Germany*
[3] *Yonsei University, Graduate School of Earth System Sciences-Astronomy-Atmospheric Sciences, Yonsei-ro 50, Seoul 120-749, Republic of Korea*

arXiv:1606.08778v1 [astro-ph.GA] 28 Jun 2016

29 June 2016

ABSTRACT

We attempt to find a progenitor for the ultra-faint object Segue 1 under the assumption that it formed as a dark matter free star cluster in the past. We look for orbits, using the elongation of Segue 1 on the sky as a tracer of its path. Those orbits are followed backwards in time to find the starting points of our N-body simulations. The successful orbit, with which we can reproduce Segue 1 has a proper motion of $\mu_\alpha = -0.19$ mas yr^{-1} and $\mu_\delta = -1.9$ mas yr^{-1}, placing Segue 1 near its apo-galacticon today. Our best fitting model has an initial mass of $6224\,\mathrm{M}_\odot$ and an initial scale-length of 5.75 pc.

Key words: galaxies: dwarfs — galaxies: individual (Segue 1) — methods: N-body simulations

1 INTRODUCTION

The Milky Way (MW) is surrounded by many dwarf spheroidal galaxies (dSph). With the advent of large surveys like for example the Sloan Digital Sky Survey (SDSS York et al. 2000) many faint and also ultra-faint dSph have been and are still discovered, increasing the number of satellites of the MW tremendously (see e.g., Laevens et al. 2015, for one of the latest discoveries).

The high velocity dispersions observed in these objects suggest the presence of a lot of dark matter (DM), if virial equilibrium and standard gravity is assumed. The assumption of virial equilibrium enables to deduce a dynamical mass for these objects (Binney & Tremaine 1987, e.g., chapter 4 in). As these dynamical masses exceed the visible mass in stars by orders of magnitude, the least luminous dwarfs are considered the most DM dominated objects in the known universe making them critical targets for indirect DM detection experiments (e.g., Baltz et al. 2000; Evans et al. 2004; Pieri L. et al. 2009; Martinez et al. 2009).

Segue 1 was discovered by Belokurov et al. (2007) as an overdensity of resolved stars in imaging data from the SDSS and the authors suggest that Segue 1 is an extended globular cluster, possibly associated with the Sagittarius stream. This interpretation was contested by Geha et al. (2009), who demonstrated that the kinematics of stars in Segue 1 clearly indicates that it is a dark matter dominated object. They measured the radial velocities of 24 stars in Segue 1 and claimed that this object is a dwarf galaxy rather than a globular cluster with a mass to light ratio of 1320. That makes Segue 1 one of the most DM dominated objects known until this day. Niederste-Ostholt et al. (2009) questioned this assumption. If Segue 1 is a globular cluster that is undergoing tidal disruption, then extra-tidal stars may not be so easy to distinguish from gravitationally bound members. Studies of Smith et al. (2013); Blaña et al. (2015, e.g.,) have shown that objects on the brink of destruction and/or close to apo-galacticon are surrounded by sufficient extra-tidal stars to boost the measured velocity dispersion by an order of magnitude or even more. This boosted velocity dispersion measurement, which does not represent the 'real' velocity dispersion of a bound object in equilibrium, will lead to a significant overestimation of the dynamical mass and therefore to the postulation of a heavily DM dominated object. Furthermore, if Segue 1 is immersed in the Sagittarius stream, the contamination of any sample of Segue 1 stars by stars of the stream may be hard to avoid.

Segue 1 is located at equatorial coordinates of $\alpha_{2000} \approx 151.77^o$, $\delta_{2000} \approx 16.08^o$ and at a distance of 23 kpc from the Sun (Belokurov et al. 2007). Its central surface-brightness is $\mu_0 = 27.6^{+1.0}_{-0.7}$ mag arcsec^{-2} and its luminosity is about $340\,\mathrm{L}_\odot$ (Martin et al. 2008). Simon et al. (2011) after correcting for the influence of binary stars using repeated velocity measurements, determined the velocity dispersion of Segue 1 to be $\sigma_{\rm los} = 3.7^{+1.4}_{-1.1}$ km s^{-1} and the radial velocity to be $v_{\rm rad} = 208.5 \pm 0.9$ km s^{-1}. The projected half-light radius is estimated to be $r_{\rm h} = 29^{+8.0}_{-5.0}$ pc.

The goal of this project is to find a progenitor, which can reproduce the observational data of Segue 1, mentioned above and shown in Tab. 1, under the assumption that Segue 1 has formed as a star cluster, i.e., as an object without its own dark matter halo. Success in this project does not mean that Segue 1 has to be a dark matter free object, it simply opens up another possibility for discussion. In our simulations we do not include any information about metalicities or star formation histories.

In the next section we explain the setup of our simulations

⋆ rdominguez@astro-udec.cl

Table 1. Observables of Segue 1, we try to reproduce in this study. Rows 1 to 6 are taken from Martin et al (2007), rows 7 and 8 are taken from Simon et al. (2011).

Observable	Symbol	Value
Right Ascension	α	151.77^o
Declination	δ	16.08^o
Distance	D	23 ± 2 kpc
Central surface brightness	μ_0	$27.6^{+1.0}_{-0.7}$ mag arcsec^{-2}
Total luminosity	L_V	340 $L_\odot$
Half-light radius	r_h	$29^{+8.0}_{-5.0}$ pc
Velocity dispersion	σ_los	$3.7^{+1.4}_{-1.1}$ km s^{-1}
Radial velocity	v_rad	208.5 ± 0.9 km s^{-1}

Table 2. Some of the possible pairs of proper motions (μ_α and μ_δ) matching the elongation of Segue 1. First column indicates the panel of Fig. 1, where we plot the different orbits. Second and third column show the proper motions while fourth and fifth column give the peri-galacticon and apo-galacticon of the orbit, respectively.

Orbit	μ_α mas yr^{-1}	μ_δ mas yr^{-1}	R_peri kpc	R_apo kpc
a	-0.19	-1.90	2.9	31.7
b	+0.10	-1.90	5.6	31.4
c	-1.30	-1.80	2.9	34.5
d	-1.50	-1.70	5.0	35.8

followed by the description of our results. We end this paper with some conclusion and a brief discussion of our results.

2 METHOD & SETUP

To determine a possible orbit for Segue 1, having only a measurement of the radial velocity at hand, we assume pairs of proper motions (μ_α and μ_δ) and perform test particle integrations of the resulting orbit in a fixed analytic Milky Way potential (Mizutani et al. 2003, and thereafter widely used as a standard representation of the MW potential). This potential is parameterised as a logarithmic halo of the form:

$$\Phi_\mathrm{halo}(r) \quad = \quad \frac{v_o^2}{2} ln(r^2 + d^2) \tag{1}$$

with $v_0 = 186$ km s^{-1}, $d = 12$ kpc and where r is the radius in kpc.

Table 3. Position and velocity of Segue 1, today and at the start of the simulations, using orbit (a).

Orbit (a)	Today	Start
t [Gyr]	0	-10
x [kpc]	19.15	11.95
y [kpc]	9.51	-9.72
z [kpc]	17.73	-0.40
v_x [km s^{-1}]	31.90	205.57
v_y [km s^{-1}]	49.79	-112.90
v_z [km s^{-1}]	103.11	-146.73

The disk is represented by a Miyamoto-Nagai potential:

$$\Phi_\mathrm{disk}(R,z) \quad = \quad \frac{GM_\mathrm{d}}{\sqrt{R^2 + (b + \sqrt{z^2 + c^2})^2}} \tag{2}$$

with $M_\mathrm{d} = 10^{11}$ M$_\odot$, $b = 6.5$ kpc, $c = 0.26$ kpc and where R is the radius within the plane in kpc and z is the height above or below the plane in kpc.

Finally the bulge is modeled as a Hernquist potential:

$$\Phi_\mathrm{bulge}(r) \quad = \quad \frac{GM_\mathrm{b}}{r + a} \tag{3}$$

using $M_\mathrm{b} = 3.4 \times 10^{10}$ M$_\odot$, $a = 0.7$ kpc and where r is the radius in kpc. The superposition of these components provides a reasonable representation of the Milky Way potential field with a circular velocity at the solar radius of $\sim$ 220 km s^{-1}.

At present, no proper motions are available for Segue 1. Niederste-Ostholt et al. (2009) tentatively presented further over-densities that may belong to the object (their figure 4). If we assume these patches are in fact parts of the tidal tails of Segue 1, they map a path in the sky, as the tails are assumed to align with the orbit. This helps us in restricting the possible pairs of proper motions. We only consider pairs of proper motions, which lead to orbits, whose path in the sky is along these tentative over-densities. Without the assumption, i.e., that we know the path in the sky, any orbit would be possible. Furthermore, we restrict the possible orbits to solutions, which are bound to the MW and discard first passages.

In Table 2 we present some of the possible pairs of proper motions, which reproduce exactly the path in the sky outlined by the patches of over densities in Niederste-Ostholt et al. (2009). In Fig. 1 we show the projected orbits based on the proper motions from Tab. 2 in the vicinity of the position of Segue 1 today. Of course there are almost infinitely more solutions to this problem. The orbits shown and used in this table have in common that Segue 1 is close to its apogalacticon today. This is the region of possible orbits where we expect to find a solution.

We tried all of these orbits, using the method described below and found that orbit (a) from Table 2 is the only one, where we can find a possible initial star cluster evolving to a final object which reproduces all observables given in Table 1.

Having established an orbit, we calculate this orbit backwards in time for 10 Gyr. This backwards calculation is done using a test-particle inside an analytic MW potential as described above.

The choice for the length of this bachwards calculation in time is rather arbitrary as we do not know the exact formation time of Segue 1. It represents a generic old object, orbiting the MW for a long time. Furthermore, it is clear that the potential of the MW was not constant during the last 10 Gyr, but rather growing with time (see for example the Via Lactea INCITE simulation of Kuhlen et al. 2008). If we assume that the MW was less massive in the past and that Segue 1 first orbited further out, closing in due to dynamical friction and the growing potential of the MW, our generic choice of time together with a constant MW potential represents an even longer time-span in reality. A more detailed description of this method and a discussion about the simulation times used can be found in Blaña et al. (2015) and references therein.

At the position (shown in Cartesian coordinates in Table 3) 10 Gyr in the past we now insert a live model representing a possible stellar progenitor of Segue 1. We model this progenitor as a Plummer sphere (Plummer 1911) with different Plummer radii R_pl and initial masses M_pl. A Plummer sphere is a widely used representation to model a young stellar cluster (e.g., Boily & Kroupa 2003). We use the particle-mesh code SUPERBOX (Fellhauer et al.

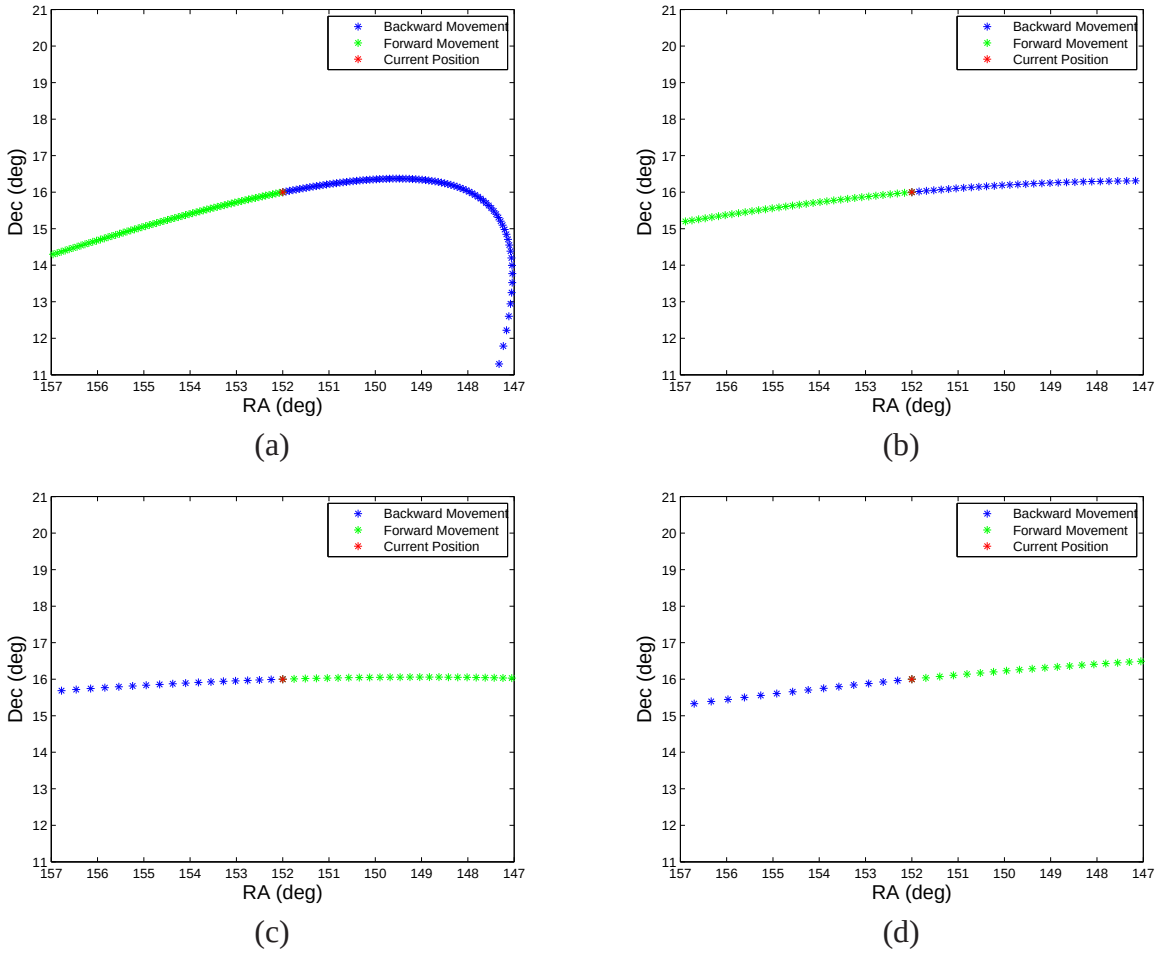

Figure 1. Path of the possible orbits from Tab. 2 shown in the sky in the vicinity of the actual position of Segue 1. Blue stars show the orbit followed backwards in time, green stars show the future orbital path. The red star denotes the position of Segue 1 today. The time-step used in these test-particle calculations is 0.01 Myr.

2000) to simulate this progenitor forward in time until we reach again the position of Segue 1 today. We analyse the final model as described in Sec. 3 and compare the data to the observables.

As we are simulating masses and not luminosities we convert our masses into luminosities using a generic stellar mass-to-light ratio of $2\,\mathrm{M}_\odot/\mathrm{L}_\odot$, e.g., we assume the total stellar mass of Segue 1 to be $680\,\mathrm{M}_\odot$. This assumption is valid as Segue 1 consists of old and metal-poor stars (Frebel et al. 2014), which have a mass-to-light ratio larger than unity.

To find a suitable progenitor model we follow closely the method described in Blaña et al. (2015). This method uses the fact that the final mass of the object, its central surface brightness, its effective radius and its internal velocity dispersion can each separately be matched by a 1D subset, i.e., a power-law function, of the initial 2D parameter space spanned by the parameters $M_{\rm pl}$ and $R_{\rm pl}$. Furthermore, it relies on the fact that each observable has a different dependency on the initial parameters, i.e., the power-laws are different for different observables. If there is a matching solution to the problem at hand, i.e., here to find a possible progenitor for Segue 1, all these power-law functions should ideally intersect in one point. Due to measurement uncertainties, the power-law functions will in practice not intersect in a single point, but in the same small region in the parameter space of initial radii and masses if there is a solution to our problem.

In contrast to other methods searching for the correct initial conditions, here, the search for a solution is performed over a wider region of parameter space instead of using an educated first guess and closing in on to the solution by trial and error. This does not necessarily mean that one has to perform less simulations in total.

3 RESULTS

From the observables listed in Table 1, the position, i.e., the right ascension, declination and distance to the Sun, and the radial velocity of the system are matched automatically by design of the simulations. The objects are simulated forward in time using a particle-mesh code. Obviously, the simulated objects should end up at the same position today, where we started our backwards test-particle calculation from. Small deviations are to be expected as a live, extended system behaves slightly different than a test-particle. These deviations (in our simulations in all three dimensions) are by an order of magnitude less than the observational uncertainty in the measured distance.

If we want to describe the results of our simulations we have to distinguish between how a single simulation evolves in time and

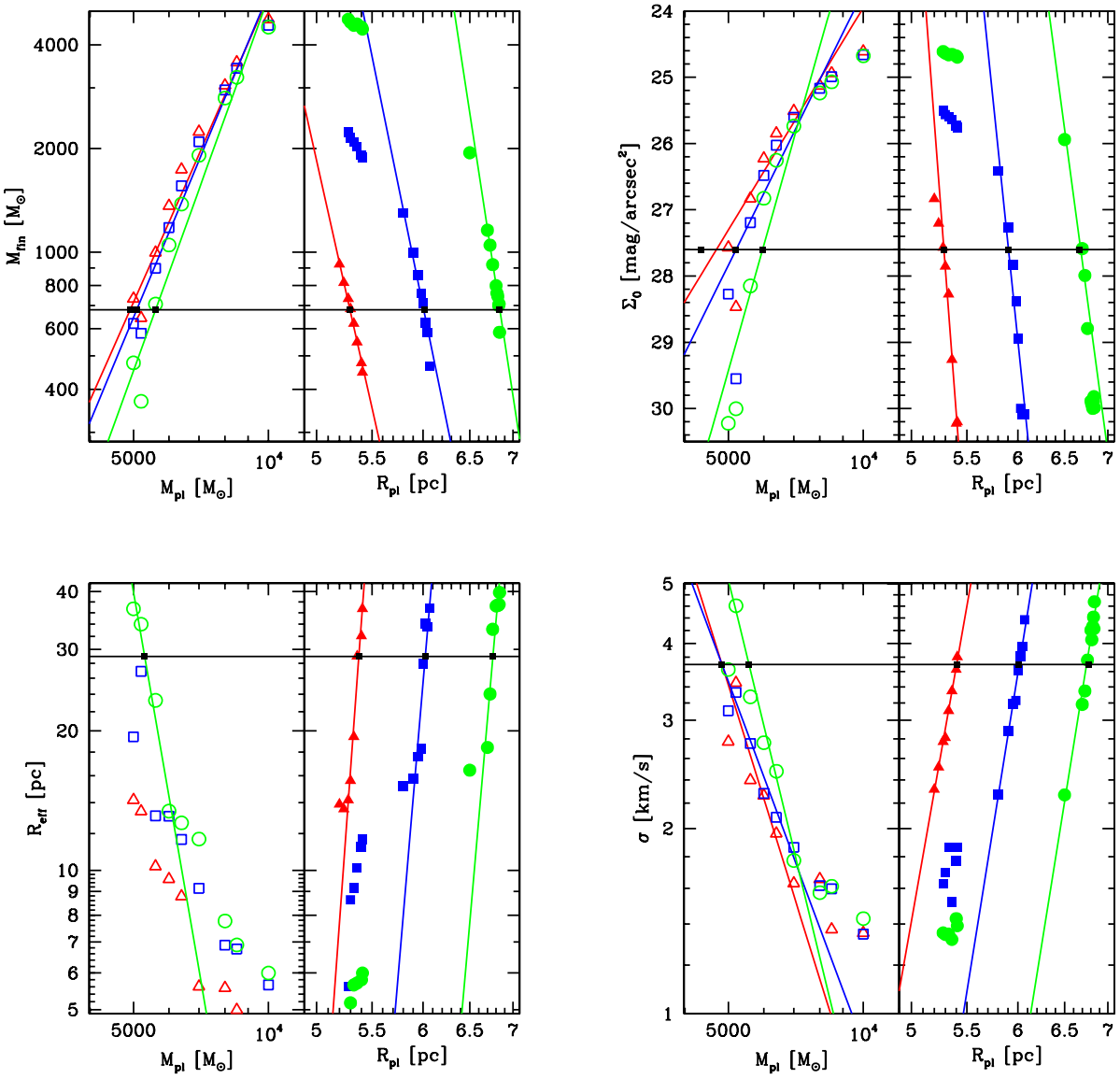

Figure 2. Final parameter (observable) as function of the initial Plummer mass $M_{\rm pl}$ for different choices of the initial Plummer radius $R_{\rm pl}$ (left part of each panel) and as a function of the initial Plummer radius for different choices of the initial mass (right part of each panel). Top left: final mass, top right: central surface brightness, bottom left: effective radius, bottom right: velocity dispersion. Left side of each panel: we show the data points and the fitting lines for Plummer radii of 5.28 (red circles), 5.30 (blue stars), 5.33 (cyan squares), 5.40 (green, crosses), and 5.41 (magenta, diamonds) pc. Right side of each panel: we show data points and fitting lines for initial masses of 1×10^4 (blue stars), 8×10^3 (red circles), 7×10^3 (cyan squares) and 5×10^3 (green crosses) solar masses . The black lines indicate the upper and lower observational limit (Tab. 2) and the line in the center indicate the central observational value of Segue 1. No observational error has been published for the mass so we only fit the inferred mass from the luminosity as was explained in section 2.

how the results of the observables, we want to match, evolve with changing the initial parameters of the simulations (keeping simulation time, orbit and Galactic potential constant).

The general trend for the evolution of a single simulation with time can be described as:

- At each peri-centre passage our object loses mass, through the Lagrangian points L1 and L2.
- Due to the mass-loss, the object expands (formation of tails) and the (central) surface brightness diminishes with time.
- The lost particles will align with the orbit, while moving out towards the apo-centre of the orbit, forming tidal tails along the orbit.
- Due to the formation of tidal tails the object will look more and more elongated.
- Particles in the tails have slightly different energies and angular momentum than the remaining bound object, i.e., they will spread out with time, forming longer and longer tidal tails.
- as velocities are lower closer to apo-galacticon, the tails will contract – the opposite happens close to peri-galacticon.
- If sufficient mass is lost (usually more than 90%; see, e.g., Smith et al. 2013) the object is at the brink of destruction and a final

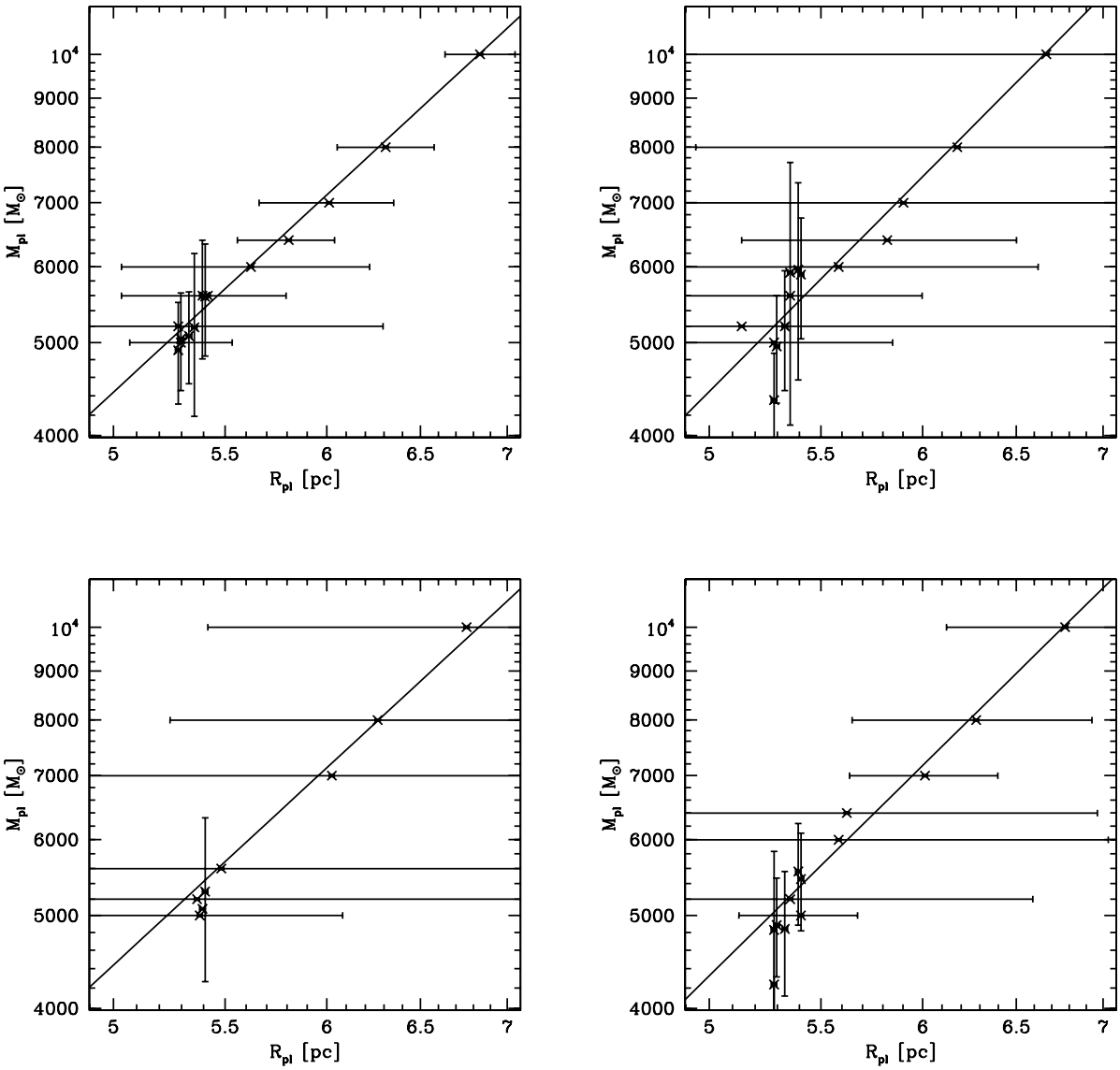

Figure 3. Data-points show the pairs of initial parameters which lead to the correct final value of the given observable. The data-points can be fitted by power-laws, describing 1D sub-sets of the initial 2D parameter space. Top left: final mass, top right: central surface brightness, bottom left: effective radius, bottom right: velocity dispersion.

peri-centre passage will completely dissolve the object, turning it into a pure stellar stream.

Now, for this study, we are more interested in the general trends, how the initial parameters influence the results of the simulations:

- The lower the initial mass is, the lower is the final mass of the object. The larger the initial Plummer radius is, the easier it is for the object to lose mass and the final mass shrinks with increasing initial Plummer radius.
- The stronger the mass-loss, the more the central surface brightness is diminished.
- In contrast the effective radius of our final object will increase, because the nearby tails will be confused with parts of the bound object.
- The velocity dispersion will become smaller with increasing mass-loss until sufficient mass is lost, that the unbound particles dominate the dispersion measurement, boosting the velocity dispersion to higher values with higher mass-loss.

We can categorise our results of the simulations in three different regimes:

- First, we have the 'bound' regime: High initial masses or very concentrated initial objects (small Plummer radius), will be less affected by the Galactic tides. Sufficient mass is still found as a bound object and the observables, we measure, are dominated by this bound object. I.e., the mass is mainly the bound mass, the central surface brightness is the one of the remaining bound object, the effective radius gets smaller, and we measure a velocity dispersion, which is only slightly affected by unbound stars.

• If the mass-loss is very high, and the object is at the brink of total destruction, then the observables are fast changing functions of the initial parameters: final mass is dropping fast with larger initial radii and/or smaller initial masses, the central surface brightness is also dropping fast, the effective radius is increasing rapidly, and so does the velocity dispersion, as it is extremely boosted by unbound stars. We dub this the 'intermediate' regime. In this regime we expect to find the correct solution.

• Finally, if all mass is lost and the object is completely destroyed, we are left with a stellar stream without an object. This happens at very low initial masses and/or very extended initial objects. We call this the 'stream' regime. Observables, measured in this regime, are almost constant and very low.

3.1 Final Mass

Of course, we cannot use the remaining bound mass of our model, as we see Segue 1 in the final stages of dissolution in our scenario. Therefore, the total luminosity determined by the observers includes the faint luminosities of the tails around the object as well. We, therefore, count all particles in a box which spans ± 0.20 degree in right ascension and ± 0.17 degree in declination from the centre, which is equivalent to the outermost luminosity contours drawn by Simon et al. (2011).

In Fig. 2 (top left panel), we show the results for the final mass ($M_{\rm fin}$) of our object. In the left half of the panel we plot these results as function of the initial Plummer mass ($M_{\rm pl}$; open symbols). Simulations with different initial radii are represented with different symbols (and colours). Red triangles represent simulations with initial Plummer radius of 5.28 pc, blue squares represent 5.33 pc, and green circles 5.41 pc. On the right half of the panel we show the final mass ($M_{\rm fin}$) of our object, now as a function of the initial Plummer radius (filled symbols). On this side different symbols (and colours) represent simulations with different initial Plummer masses. Red triangles represent simulations starting with $M_{\rm pl} = 5 \times 10^3$ M$_\odot$, blue squares 7×10^3 M$_\odot$, and green circles 10^4 M$_\odot$.

In these double-logarithmic plots most if not all results for a given $R_{\rm pl}$ on the left and for a given $M_{\rm pl}$ on the right can be fitted with a single straight line, i.e., a power-law function. These fitting lines are shown in the same colour as their data-points. We see that in the right half of the panel the results in the upper part are deviating from the power-law. This behaviour, described already in Blaña et al. (2015), stems from results which belong to the first regime of resulting objects, i.e., here we have bound objects which lose only part of their initial mass. Furthermore, it is clear that the power-laws on this side of the panel can not extend to final masses, which are higher than the initial ones. Naturally, we exclude those deviating results from the fit.

Having established that for each constant initial radius and for each constant initial mass we can fit a power-law to the results (final mass as function of the initial mass on the left and final mass as function of the initial scale-length on the right), we can determine the intersections of these power-laws with the horizontal line denoting the correct final mass, we assume for Segue 1 (680 M$_\odot$). This gives us pairs of initial conditions, where our simulations would lead to the correct final mass for Segue 1. In the plot these are denoted by small black squares. If we now plot all these possible solutions for the correct final mass into a plot of initial mass versus initial scale-length as done in the top left panel of Fig. 3, we again note that all these possible solutions are following a straight line in a double-logarithmic plot, i.e., they can be fitted by a power-law of the form:

$$M_{\rm pl} \quad = \quad 67.6^{+8.3}_{-7.3} \times R_{\rm pl}^{2.60 \pm 0.06}. \qquad (4)$$

This equation describes the 1D subset of initial parameters (from the 2D parameter space of initial conditions) that leads to the assumed observed value of the mass of Segue 1.

3.2 Central surface brightness

As the final objects in our simulations span the range from perfectly bound objects to completely destroyed ones, i.e., pure stellar streams, there is no simple radial profile, which could fit all the data of all simulations. We therefore produce pixel-maps with a 20 pc resolution per pixel and determine the brightness of the densest pixel, which we consider the centre of our object. As explained above, objects become larger with simulation time, this 20 pc resolution has nothing to do with the initial scale-lengths used for our models (in the order of 5 to 6 pc). It rather represents the resolutions found with star count contours of dSph galaxies observations in the MW (Irwin & Hatzidimitriou 1995, see for example).

Plotting the central surface brightness of our objects as function of the initial parameters in Fig. 2 (top right panel, symbols, colours and lines are the same as explained above), we fit power-laws to the data-points in the intermediate region and determine again which initial Plummer radius leads to the correct central surface brightness for a given initial mass and which initial mass leads to the correct central surface brightness for a given initial radius. The data-points obtained from these fits are shown in the top right panel of Fig. 3. The fitting line (power-law) to these data points is

$$M_{\rm pl} \quad = \quad 46.8^{+10.7}_{-8.8} \times R_{\rm pl}^{2.83 \pm 0.11}. \qquad (5)$$

This power-law describes all pairs of initial parameters which lead to final objects, matching the central surface brightness of Segue 1.

3.3 Effective radius

To determine the effective radius we have no other choice than to fit single Sersic profiles to our simulation data, without making a distinction between bound and unbound particles (see previous section). We exclude the central region, which may be dominated by a bound remnant, and we also exclude the far away tidal tails, as they are too faint to be detected observationally.

Our fits show Sersic indices which are close to 1. This is equivalent to an exponential profile which is observed with most dSph galaxies.

We see in Fig. 2 (bottom-left panel) that the final effective radius increases with the initial Plummer radius (right half). In the 'bound regime' the increase is slow and reflects the simple fact that we start with more extended objects. In the intermediate region the effective radius increases fast as more and more material is in the tidal tails and the remaining bound object expands as well. Finally, once only a stream is left, the increase levels off as now we measure the extent of the stream rather than a meaningful profile.

Using the same procedure as described before we show the resulting data in the lower left panel of Fig. 3 and describe the fitting line as:

$$M_{\rm pl} \quad = \quad 39.81^{+6.96}_{-5.93} \times R_{\rm pl}^{2.88 \pm 0.10}. \qquad (6)$$

3.4 Velocity dispersion

To determine the velocity dispersion, we calculate the total velocity dispersion using the radial velocities of all particles within the same box, we used to determine the final mass. This is also the region, where most of the stars are found, which were used to determine the velocity dispersion observationally.

The results in Fig. 2 (bottom-right panels) show for a given initial mass as function of the initial radius first a decreasing dispersion with increasing radius and then a turn around and an increase steeply with increasing initial radius (right-panel). This behaviour can be understood as follows: First, we measure the velocity dispersion of the bound object (with only a small contamination of unbound stars), which decreases as the final object is less and less massive. At one point the velocity dispersion gets dominated by unbound stars and is increasing again, as unbound stars are on different orbits around the Galaxy and we measure a distribution of epicyclic frequencies rather than a real velocity dispersion. In this region, where the velocity dispersion is boosted by unbound particles, we determine our power-laws. The results are shown in the lower right panel of Fig. 3 and can be described as:

$$M_{\rm pl} \quad = \quad 50.1^{+16.0}_{-12.1} \times R_{\rm pl}^{2.77\pm0.16}. \qquad (7)$$

One could now ask how robust is our measurement of the velocity dispersion and if we do include particles, which observers would reject as interlopers or unbound, thereby inflating our dispersion to the desired high values. We repeat the analysis on our best fitting model (see next section) with different observational methods as described in Smith et al. (2013) and find all methods to lead to extremely boosted velocity dispersions.

It is very easy for us to determine which particles of our simulation are still bound to each other. If we determine their line-of-sight velocity dispersion of the bound particles alone (and only with this velocity dispersion the virial theorem applies) we obtain $\sigma_{\rm bound} = 0.29$ km s^{-1}. This shows clearly that velocity dispersions can be severely boosted by unbound particles.

With the method we use, i.e., to take the projected velocities of all the particles in the same box where we measure the final mass, our analysis gives us a velocity dispersion of $\sigma_{\rm los} = 3.52$ km s^{-1}. Now, our sample only contains particles ('stars') which belong or used to belong to the object. In a simulation we do not have contamination from random halo stars, which happen to be in the same field of view. We mimic a three-sigma-clipping algorithm used by Yahil & Vidal (1977) to reject interlopers (which are not present) and obtain a somewhat lower dispersion of $\sigma_{\rm clip} = 2.20$ km s^{-1}. If we apply the new interloper rejection technique (IRT) described by Klimentowski et al. (2007), we arrive at a somewhat higher value of $\sigma_{\rm IRT} = 3.91$ km s^{-1}. Even though those three methods do not agree very well with each other, they all show a boosted dispersion by an order of magnitude compared to the bound particles alone. As shown in e.g., Smith et al. (2013) the boosting is higher the closer the object is to destruction and the closer we see the object to its apo-galacticon, when the tails get compressed. Both effects are at work at our solution for Segue 1.

3.5 Best fitting model

Having established how the four observables depend on our initial parameters, we now have a look, if our solutions converge towards a single solution. We show the different fitting lines from Fig. 3 together in the panels of Fig. 4. We see clearly that the lines intersect but not at the same point. This would only be the case in an absolute ideal world, where none of the observables would have any error margin (and of course if a solution exits). Taking the one sigma deviations into account, published for the different observables (excluding final mass as here we have no handle on the error stemming from determining the total visual magnitude and then transforming it into a mass using a rather generic mass-to-light ratio), we obtain a small region in initial parameter space in which all observational quantities are matched within their observational one sigma errors (shown as red crosses in the right panel of Fig. 4). We place our best-fitting model in the centre of this small area using an initial Plummer radius of $R_{\rm pl} = 5.75$ pc and an initial mass of $M_{\rm pl} = 6224$ M$_\odot$.

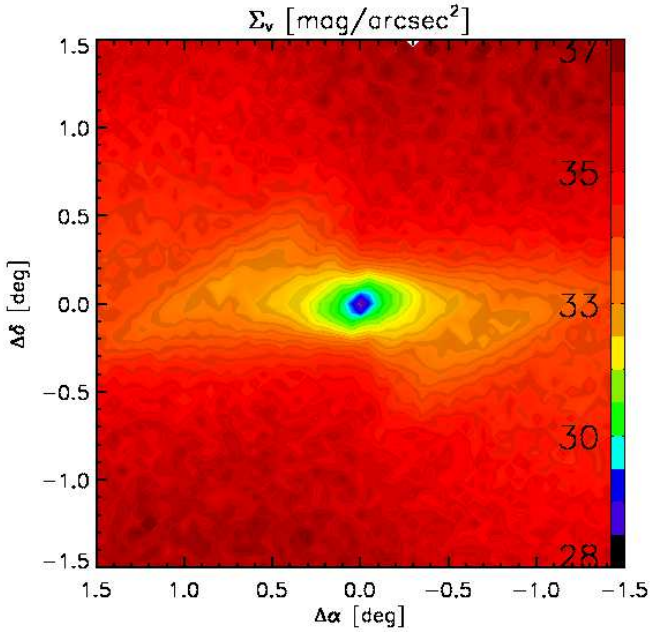

Figure 5. Surface brightness contours of our best fitting model, resembling Segue 1.

Running a last simulation with these initial parameters leads to a final object for which we show the surface brightness contours in Fig. 5. It has the correct elongation and shows faint tails, which may have been picked up in the study of Niederste-Ostholt et al. (2009). The blue regions in the figure represent surface brightnesses, brighter than 30 mag arcsec^{-2}, which are now possible to observe via star counts. The green, yellow and orange regions have very low surface brightnesses and may get picked up by chance. They are located in the same places as the tentative patches of Niederste-Ostholt et al. (2009). All the red and dark red regions have brightnesses fainter than about 35 mag arcsec^{-2} and are impossible to observe. In our simulations we have maybe a handful of particles (phase-space elements) per pixel in those areas, which would represent less than one observable star per pixel in reality.

We obtain for this best fitting model the following 'observables':

(i) A final mass of 686^{+28}_{-52} M$_\odot$ measured in the region described above.
(ii) A central surface brightness of $\mu_0 = 28.4^{+0.8}_{-0.3}$ mag.
(iii) An effective radius of $26.6^{+3.8}_{-3.7}$ pc.
(iv) A line-of-sight velocity dispersion of $3.29^{+0.12}_{-0.31}$ km s^{-1}.

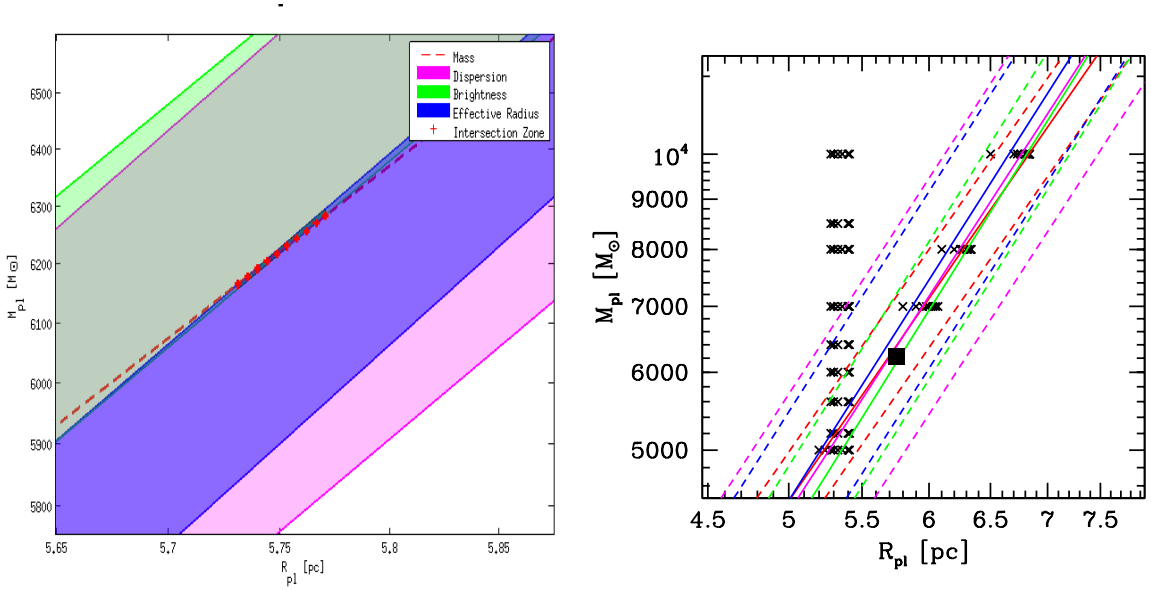

Figure 4. Joining all power-law fits from Fig. 3 in one single graph. Left panel shows shaded areas representing the observational uncertainties for the observational quantities (except mass here we cannot address the error; see main text). In the right panel we show the fitting lines (solid) together with the mathematical errors (1σ) as dashed lines. Red lines for the mass, blue for the surface-brightness, green for the effective radius and magenta for the velocity dispersion. In an ideal world all lines should intersect in one point, where the correct initial conditions of Segue 1 should be found. Instead the lines intersect inside a small region. In the left panel this region is denoted with red crosses; in the right panel we show a big black square where we place our best fitting model. Furthermore, the right panel shows all initial conditions of our simulations as black crosses.

These values are in very good agreement with the observed quantities shown in Table 1.

4 CONCLUSION & DISCUSSION

We have embarked on a project to find a non dark matter dominated progenitor for the Segue 1 dSph. With our simulations we could show that assuming an orbit with proper motions of $\mu_\alpha = -0.19$ mas yr^{-1} and $\mu_\delta = -1.9$ mas yr^{-1} ($R_{\rm peri} = 2.9$ kpc, $R_{\rm apo} = 31.7$ kpc), which places the object near its apo-galacticon today, we are indeed able to reproduce all observables dealing with kinematics.

The choice of our orbit relies heavily on our assumption that the patches of stars observed by Niederste-Ostholt et al. (2009) are indeed parts of the tidal tails of Segue 1. If this assumption is false, then the choice of orbit becomes completely arbitrary (as long as the orbit matches the determined radial velocity). On the other hand, assuming any orbit would make it much easier to find a suiteable one in which we see Segue 1 close to its apo-galacticon, at the final stages of destruction and on top of that in the favourable position that we look partly along the tidal tails to have a better boosting of the velocity dispersion. So, while our restriction of the path of the orbit leads to a precise prediction of the initial conditions, we need to reproduce the observables of Segue 1, a total freedom of the orbit would give us more and easier possibilities to find matching solutions.

Using a Plummer sphere as initial model, we find that the progenitor of Segue 1 can be a small star cluster that formed 10 Gyr ago with a scale-length of less than 6 pc and an initial mass of about 6×10^3 M$_\odot$. Today, Segue 1 has, according to our model, lost most of its mass, it is at the brink of destruction, and it is located close to its apo-galacticon. Therefore, we see an extremely boosted velocity dispersion (more than an order of magnitude) stemming almost entirely from unbound stars.

This study shows that from a kinematical and structural point of view, it is indeed possible to explain Segue 1 as a completely dark matter free entity, without invoking new physics like MOND. It is, on the other hand, very straightforward to explain Segue 1 as a highly DM dominated object. One just takes the kinematical observables, assumes virial equilibrium and obtains a mass-to-light ratio which is impossible to explain by a pure stellar population alone. Models like Assmann et al. (2013a,b) show that most if not all kinematical peculiarities of dSph galaxies (e.g., elongations, off-centre nuclei, twisted contours, cold sub-populations, etc.) can be explained by clustered star formation inside of DM haloes. These models work without the need for any additional perturbations from the MW or other galaxies. It is therefore not difficult to explain Segue 1 as a DM dominated dwarf galaxy, and even though this might be the correct answer, this in not part of this study, which is looking for the possibility to find an alternative explanation, which we have.

Our model lacks one big ingredient. We are using a particle-mesh code to simulate a small star cluster, thereby neglecting completely the internal evolution of the star cluster and the resulting mass-loss due to two-body relaxation. These fast models allow us to cover a vast parameter space of initial conditions on various orbits, while direct N-body simulations, even though possible for objects similar to our initial models, are time-consuming and require special hardware.

Fellhauer et al. (2007) showed that, in the case of NGC 5466, the mass-loss due to the Galactic potential is about 60% of the the total mass lost, including two-body relaxation and stellar evolution. In the case of Segue 1, due to its orbit closer to the Galactic centre, we expect this percentage to be even higher. Nevertheless, one should regard our initial mass of Segue 1 as a lower limit, as it ne-

glects stellar evolution and relaxation effects. The 'birth' mass may even be much higher, as stellar evolution in the first few Myr is fast and coupled with a strong mass-loss (e.g., Supernovae and/or stellar winds of high mass stars). If additionally effects like gas-expulsion of an embedded young cluster is taken into account, depending on a completely unknown star formation efficiency, the real initial mass is completely unknown. Our initial mass represents, at best, a lower limit for a gas-free star cluster, after the violent and fast initial evolution, i.e., a couple of tens of Myr after its birth.

One other caveat, is the metalicity spread observed in Segue 1, which is higher than expected from any DM free star cluster. In our study we focus on the kinematics alone. In a particle-mesh code, particles represent phase-space elements and not stars. Therefore, this study cannot give an explanation for any star formation and/or chemical enrichment history of Segue 1. Our study only shows, that it is possible to reproduce all kinematical and structural properties of Segue 1 with a DM free model.

Acknowledgments: MF acknowledges financial support of FONDECYT grant no. 1130521 and BASAL PFB-06/2007. RD and JPF are partly funded through a studentship of FONDECYT grant no. 1130521. JPF acknowledges funding through a CONICYT studentship for Magister students. JD is funded through FONDECYT grant no. 3140146 and GNC is funded through FONDECYT grant no. 3130480.

REFERENCES

Assmann P., Fellhauer M., Wilkinson M.I., Smith R. 2013, MNRAS, 432, 274
Assmann P., Fellhauer M., Wilkinson M.I., Smith R., Blaña M. 2013, MNRAS, 435, 2391
Baltz E.A., Briot C., Salati P., Taillet R., Silk J. 2000, PhysRevD, 61, 3514
Belokurov V., et al. 2007, ApJ, 654, 897
Binney J., Tremaine S. 1987, 'Galactic Dynamics', Princeton Series in Astrophysics, ISBN 0-691-08445-9
Blaña M., Fellhauer M., Smith R., Candlish G.N., Cohen R., Farias J.P. 2015, MNRAS, 446, 144
Boily C.M., Kroupa P. 2003, MNRAS, 338, 673
Evans N.W., Ferrer F., Sarkar S. 2004, PhysRevD, 69, 123501
Fellhauer M., Kroupa P., Baumgardt H., Bien R., Boily C.M., Spurzem R., Wassmer N. 2000, New Ast., 5, 305
Fellhauer M., Evans N.W., Belokurov V., Wilkinson M.I., Gilmore G. 2007, MNRAS, 380, 749
Frebel A., Simon J.D., Kirby E.N. 2014, ApJ, 786, 74
Geha M., Wilman B., Simon J.D., Strigari L.E., Kirby E.N., Law D.R., Strader J. 2009, ApJ, 692, 1464
Irwin M., Hatzidimitriou D. 1995, MNRAS, 277, 1354
Kuhlen M., Diemand J., Madau P., Zemp M. 2008, Journal of Physics: Conference Series, Vol. 125, Issue 1, p.1
Laevens B.P.M. et al. 2015, ApJ submitted, arXiv:1507.07564
Martinez G.D., Bullock J.S., Kaplinghat M., Strigari L.E., Trotta R. 2009, JCAP, 06, 14
Martin N.F., Ibata R.A., Chapman S.C., Irwin M., Lewis G.F. 2007, MNRAS, 380, 281
Martin N.F., de Jong J.T.A., Rix H.-W. 2008, ApJ, 684, 1075
Mizutani A., Chiba M., Sakamoto T. 2003, ApJ, 589, 89
Niederste-Ostholt M., Belokurov V., Evans N.W., Gilmore G., Wyse R.F.G., Norris J.E. 2009, MNRAS, 398, 1771
Pieri L., Pizella A., Corsini E.M., Dalla Bontà E., Bertola F. 2009, A&A, 496, 351
Plummer H.C. 1911, MNRAS, 71, 460
Simon J.D. et al. 2011, ApJ, 733, 46
Smith R., Fellhauer M., Candlish G.N., Wojtak R., Farias J.P., Blaña M. 2013, MNRAS 398, 1771
York D.G., et al. 2000, AJ, 120, 1579
Klimentowski, J., et al. 2007, MNRAS, 378, 353
Yahil, A., & Vidal, N. V. 1977, ApJ, 214, 347

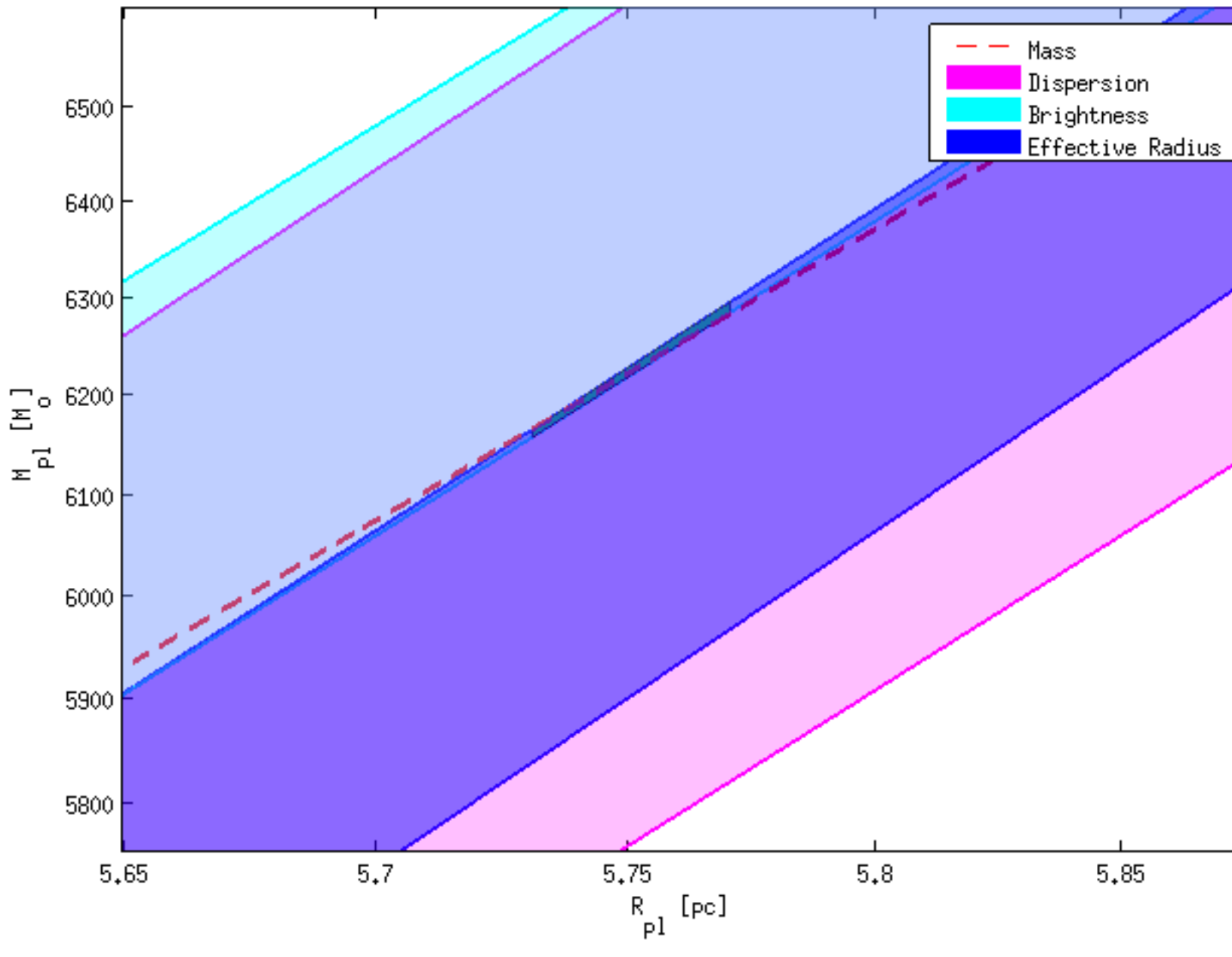
Mass
Dispersion
Brightness
Effective Radius
6500
6400
6300
6200
6100
6000
5900
5800
M_pl [M_o]
5.65
5.7
5.75
5.8
5.85
R_pl [pc]